Delineating environmental control of phytoplankton biomass and phenology in the Southern Ocean

Mathieu Ardyna, Hervé Claustre, Jean-Baptiste Sallée, Francesco d'Ovidio, Bernard Gentili, Gert van Dijken, Fabrizio d'Ortenzio, Kevin Robert Arrigo

Delineating environmental control of phytoplankton biomass and phenology in the Southern Ocean

Authors: Mathieu Ardyna[1]*, Hervé Claustre[1], Jean-Baptiste Sallée[2], Francesco d'Ovidio[2], Bernard Gentili[1], Gert van Dijken[3], Fabrizio D'Ortenzio[1], Kevin Arrigo[3]

Affiliations:
[1]Sorbonne Universités, UPMC Univ Paris 06, INSU-CNRS, Laboratoire d'Océanographie de Villefranche, 181 Chemin du Lazaret, 06230 Villefranche-sur-mer, France

[2]Sorbonne Universités, UPMC Univ Paris 06, CNRS-IRD-MNHN, LOCEAN Laboratory, 4 Place Jussieu, Paris F-75005, France

[3]Department of Earth System Science, Stanford University, Stanford, California, USA

Main point #1: Phytoplankton phenology and biomass are mostly organized in the Southern Ocean at a large latitudinal scale and a regional scale.

Main point #2: The timing of bloom occurrence appears tightly linked to the seasonal cycle in irradiance, with some exceptions in specific light-limited regimes.

Main point #3: Zonal asymmetries in regional-scale phytoplankton biomass are mainly driven by local advective and iron supply processes.

Running head (40 characters max): Phytoplankton dynamics in the SO

Keywords: Phytoplankton ecology, Phytoplankton phenology, Biological pump, Climate Change, Southern Ocean, Remote sensing.

*Correspondence to: Mathieu.Ardyna@obs-vlfr.fr.

To be submitted to *Geophysical Research Letters*

Abstract

The Southern Ocean (SO), an area highly sensitive to climate change, is currently experiencing rapid warming and freshening. Such drastic physical changes might significantly alter the SO's biological pump. For more accurate predictions of the possible evolution of this pump, a better understanding of the environmental factors controlling SO phytoplankton dynamics is needed. Here we present a satellite-based study deciphering the complex environmental control of phytoplankton biomass (PB) and phenology (PH; timing and magnitude of phytoplankton blooms) in the SO. We reveal that PH and PB are mostly organized in SO at two scales: a large latitudinal scale, and a regional scale. Latitudinally, a clear gradient in the timing of bloom occurrence appears tightly linked to the seasonal cycle in irradiance, with some exceptions in specific light-limited regimes (i.e. well-mixed areas). Superimposed on this latitudinal scale, zonal asymmetries, up to three orders of magnitude, in regional-scale PB are mainly driven by local advective and iron supply processes. These findings provide a global understanding of PB and PH in SO, which is of fundamental interest for identifying and explaining ongoing changes as well as predicting future changes in the SO biological pump.

1. Introduction

The Southern Ocean (SO) plays a key role in the global carbon cycle, absorbing 40% of the total oceanic inventory of anthropogenic CO_2 [*Khatiwala et al.*, 2009]. However, current and predicted changes in ocean circulation and hydrology associated with climate variability might impact the efficiency of the SO carbon sink, although the extent of such changes and their specific impact on the biological pump are still vigorously debated [*Landschützer et al.*, 2015; *Le Quéré et al.*, 2010; *Munro et al.*, 2015]. Such debate cannot advance without a better

69 understanding of the factors that shape the complex biogeography of the SO, and what controls
70 their time-scale of variability (i.e. daily, seasonal to decadal).

71 Delimiting marine bio-regions has proven highly valuable for disentangling multiple
72 limiting growth factors affecting the efficiency of the biological pump [*Longhurst*, 2007]
73 mediated by both PB and PH, and for ultimately underlining effects of climate change such as
74 areal changes in trophic regime [*Polovina et al.*, 2008] or in fisheries stock and species
75 [*Fossheim et al.*, 2015]. Changes in PB profoundly alter the efficiency of the biological pump,
76 thereby modulating energy transfer to upper trophic levels and carbon export to deep water
77 [*Legendre and Rassoulzadegan*, 1995]. Changes in PH may also have important consequences
78 for the marine food web, due to potential mismatch between primary and secondary producers
79 and apex predators [*Ardyna et al.*, 2014; *Edwards and Richardson*, 2004], and for the carbon
80 cycle through export of unexploited carbon aggregates to the deep ocean [*Dall'Olmo et al.*,
81 2016].

82 The efficiency of the SO's biological pump is strongly associated with phytoplankton
83 biomass (PB) and its phenology (PH), which themselves are mediated by nutrient availability
84 (e.g. mainly iron, and/or possibly nitrate and silicic acid), light, temperature and mortality factors
85 [*Behrenfeld and Boss*, 2014; *Boyd*, 2002]. These factors are essentially controlled by vertical
86 mixing, advection, seasonal fluctuations in solar irradiance, and the extent and typology of sea-
87 ice cover. As a result, a variety of patterns of net primary production (NPP) are found in the SO
88 [*Arrigo et al.*, 2008], with their own associated phytoplankton species succession, stock, and
89 distribution [*Quéguiner*, 2013]. Delineating the interplay of environmental forcing on PB and PH
90 remains challenging and requires novel approaches, which are available through satellite-derived
91 observations. Using these integrative and multidisciplinary approaches (i.e. satellite-derived

ocean color and altimetry, Argo floats, lagrangian modeling and biogeographic-derived analysis), we provide here a global understanding of the phytoplankton biomass and phenology in a potentially changing SO.

2. Material and methods

2.1 Satellite-derived, climatological and modeling products

Satellite-derived Level-3 data sets of chlorophyll-a concentration (chl *a*; mg m^{-3}) and photosynthetically available radiation (PAR; E m^{-2} d^{-1}) were obtained from the European Space Agency's GlobColour project (http://www.globcolour.info). Eight-day composite chl *a* concentrations using standard Case 1 water algorithms were used (i.e. OC4v5 for SeaWIFS, OC4Me for MERIS and OC3v5 for MODIS/VIIRS sensors; see *O'Reilly et al.* [2000] and *Maritorena et al.* [2010] for details). The climatological annual net primary production (NPP) was derived from the adapted-SO NPP model of *Arrigo et al.* [2008]. A detailed description of the NPP model can be found in the supporting information [*Dobson and Smith*, 1988; *Gregg and Carder*, 1990; *Markus*, 1999]. The climatologies of mixed layer depth and bathymetry were extracted respectively from *Pellichero et al.* [2016] and the GEBCO, version 2014 (General Bathymetric Chart of the Oceans; http://www.gebco.net). The climatology of the length of the sea-ice cover was derived from the Special Sensor Microwave Imager (SSMI; 1998–2002) and the Advanced Microwave Scanning Radiometer - Earth Observing System (AMSR-E; 2002–2014) sensors, and made available by National Snow and Ice Data Center (NSIDC; https://nsidc.org). The locations of the major fronts (i.e. the Subantarctic Front SAF, the Antarctic Polar Front APF, the Southern Antarctic Circumpolar Current (ACC) Front SACCF and the Southern Boundary of the ACC SBdy, following *Swart et al.* [2010]) were determined based on the Maps of Absolute Dynamic Topography (MADT) product from CLS/AVISO. The

Lagrangian model of horizontal dispersion of iron fluxes used also altimeter products produced by CLS/AVISO, with support from the CNES (Centre National d'Etudes Spatiales; http://www.aviso.altimetry.fr/duacs/).

2.2. Clustering K-means method

The bio-regions were defined here using a cluster K-means analysis (see the SI for more details), previously applied successfully in the Mediterranean Sea [*D'Ortenzio and Ribera d'Alcalà*, 2009; *Mayot et al.*, 2016], in the North Atlantic [*Lacour et al.*, 2015] and at the global scale [*D'Ortenzio et al.*, 2012]. The analysis was performed on climatological and normalized annual chl *a* cycle, in order to statistically organize the GLOBcolour time series (1998–2014) and to create clusters representing regions of similarity (i.e. annual chl *a* cycles). To maintain consistency in the seasonal data availability throughout the study area, the period study covers the period from September to March (as referred here to "annual"). This technique regroups pixels with seasonal cycles shapes - i.e. similar phenologies. A single characteristic seasonal cycle, that is statistically representative of the group as a whole, is then determined by calculating the center (average cycle) within each group or cluster. Each group representative of a characteristic seasonal cycle constitutes a phenological characteristic regime. A more detailed discussion of the cluster K-means analysis can be found in the supporting information [*Devred et al.*, 2007; *Hartigan and Wong*, 1979; *IOCCG*, 2009; *Lund and Li*, 2009; *Milligan and Cooper*, 1985]

A one-way analysis of variance by ranks (Kruskal–Wallis H test; *Zar* [2010]) was performed to test whether eco-regions differed in their biological characteristics (i.e. annual mean chlorophyll *a* concentration, seasonality and timing of bloom). A significant result of the Kruskal–Wallis H test implies that at least one eco-region differs from all others.

2.3 Lagrangian modeling of horizontal iron fluxes

In order to estimate iron delivery due to horizontal stirring, we use an advection scheme based on altimetry, extending to the Southern Ocean a Lagrangian model used for predicting the development of the Kerguelen phytoplanktonic plume [*d'Ovidio et al.*, 2015]. The model has been extensively calibrated and validated in the Crozet and Kerguelen regions by integrating satellite data (altimetry and ocean color), lithogenic isotopes, iron measurements, and drifters [*d'Ovidio et al.*, 2015; *Sanial et al.*, 2014; *Sanial et al.*, 2015]. The main characteristics of the model were resumed here and we refer to *d'Ovidio et al.* [2015] for the full description of the model. The model seeds each open ocean location with a particle and finds the particle's most recent contact with a shallow bathymetry by a back-trajectory issued from altimetry data. It provides the time and the position at which the contact took place. An exponential scavenging relation (with a time constant based on in situ iron data from the KEOPS2 cruise) is used to estimate the decreasing of bio-available iron along the trajectory from the time of the contact with the potential iron source to the current position. Here, the model was applied to the entire Southern Ocean using a grid of 0.25°, a time window of 2004-2015 (one map every 4 days), potential sources of iron in the bathymetric band shallower than 500m, and a diffusion term of 40 m^2 s^{-1}.

3. Results and discussion

Based on satellite-derived observations, a large range of both annual mean chlorophyll *a* (chl *a*) concentration and net primary production (NPP) (>0.1 mg chl *a* m^{-3}/20 g C m^{-2} y^{-1} to more than 2 mg chl *a* m^{-3}/400 g C m^{-2} y^{-1}, respectively) were observed across the SO. It occurs at a variety of scales, including the latitudinal and the regional (i.e. Indian, Pacific and Atlantic;

161 Fig. 1a) scales in the SO. The annual mean chl *a* concentration is associated with the amplitude
162 of its seasonal cycle (Fig. 1a&c). In contrast, the timing of blooms (i.e. the maximum of the
163 annual chlorophyll cycles, Fig. 1d) appears entirely decoupled from both large-scale patterns in
164 annual chl *a* concentration and its seasonality (Fig. 1c), hence revealing a complex organization
165 of phenological patterns of the chl *a* annual cycle.

166 Here, we disentangle the spatial complexity of chl *a* seasonal cycle using a K-mean
167 clustering method [*D'Ortenzio et al.*, 2012] with the goal of defining distinct bio-regions with
168 similar large-scale patterns in PH (Fig. 2). In brief, this technique statistically gathers regions
169 that exhibit similarly shaped seasonal chl *a* cycles (see the section 2.2 for more details). The
170 seven distinct bio-regions so identified are distributed along a latitudinal gradient (Fig. 3a). At
171 temperate latitudes, two bio-regions (i.e. 1 and 2) exhibit an early bloom in October. Moving
172 south to 45-63°S, two other bio-regions (i.e. 4 and 5) display an annual chl *a* cycle with a
173 delayed bloom in November/December. Finally, near the Antarctic continental shelf (< 63°S),
174 the dominant bio-regions 6 & 7 were characterized by a late bloom in January/February.
175 Interestingly, one bio-region (i.e. 3) differs drastically from the general phenological trend of a
176 delayed bloom moving from subtropical to polar latitudes, having a late bloom at a moderate
177 latitude (≈ 43°S, Fig. 2 & 3d). Furthermore, the co-existence of bio-regions at a same latitude
178 indicates variations in the seasonality of the annual chl *a* cycle (e.g., 1 & 2, 4 & 5 and 6 & 7)
179 which are related to distinct levels of PB (Figs 3b-c).

180 From temperate to high latitudes, the latitudinal gradient in bloom timing clearly follows
181 changes in light regime (expressed as the annual mean photosynthetically available radiation in
182 the double boxplot; Fig. 4a). The unique bio-region (i.e., 3), characterized by a paradoxically late
183 bloom with respect to the timing of light availability, is mainly located in the vicinity of the

184 Antarctic Circumpolar Current. Interestingly, this region corresponds to the highest Southern
185 Ocean wind stress and depth of the mixed layer (see SI, Fig. S1). Deep mixed-layers likely
186 impose severe light limitation to phytoplankton growth in spring, hence delaying the bloom later
187 in season. Close to the Antarctic shelf, as shown locally in the western Antarctic Peninsula
188 [*Venables et al.*, 2013], the timing of the bloom (Fig. 2) was not related to winter sea-ice extent
189 but more to the seasonal cycle of irradiance.

190 To address the potential causes of regional-scale variability in PB (Fig. 1a), we hypothesize
191 that iron availability represents its first order driver [*Hutchins and Boyd*, 2016]. Using integrative
192 and multidisciplinary approaches, we disentangle the impact of four important iron supply
193 mechanisms on PB. These surface-layer iron-sources are shallow plateaus (<500 m) which both
194 (i) locally recharge the surface-layer in iron [*Arrigo et al.*, 2015; *Graham et al.*, 2015] and (ii)
195 remotely recharge the surface layer by lateral advection of non-consumed iron [*d'Ovidio et al.*,
196 2015; *Graham et al.*, 2015]; (iii) sea-ice, which recharges the surface as ice melts [*Arrigo et al.*,
197 2015; *Lannuzel et al.*, 2016]; and (iv) vertical mixing through deep convection, which can
198 entrain iron from deep water [*Tagliabue et al.*, 2014b]. Below, the potential impact of these four
199 likely iron-sources on the intensity of PB is investigated. Note that the Aeolian iron deposition
200 was not considered here as a major iron supply mechanism due to its intermittency and its
201 unclear role in regulating PB [*Boyd et al.*, 2012; *Cassar et al.*, 2007; *Tagliabue et al.*, 2009;
202 *Tagliabue et al.*, 2017].

203 Clearly, the highest PB (> 1.2 mg m^{-3}) are detected in shallow areas (< 500 m), on
204 continental and island shelves where iron fluxes are expected to be significant [*Boyd et al.*, 2012;
205 *Tagliabue et al.*, 2014a]. Furthermore, we use a Lagrangian model based on altimetry in order to
206 track which water parcels have been recently in contact with a shallow area – and when – to

assess the probable locations of some of the iron plumes downstream of these iron sources and to estimate their loss of bio-available iron during advection by scavenging [*d'Ovidio et al.*, 2015]. We find a well-defined decline in PB (from 0.8 to 0.3 mg m^{-3}) with distance and time from the most recent contact of the water parcel with a shallow area (Fig. 4b): the further away a water-parcel is from the initial shallow area iron source, or the longer after a water-parcel has been iron-enriched in shallow areas, the weaker is the PB signal. We note however that seamounts and submerged plateaus do not enhance local or downstream PB, as already observed north of Kerguelen plateau [*Graham et al.*, 2015] (Figs. 1a&4c), suggesting that not all shallow areas are active and/or bioavailable iron sources. Close to the Antarctic shelf and coastal polynyas, the potential role of the seasonal melting of sea-ice [*Arrigo et al.*, 2015; *Lannuzel et al.*, 2016] as iron source is revealed with enhanced PB (≈0.4 mg m^{-3}).

Moving away from potential iron delivery from shallow areas (either locally or downstream) and from sea-ice, we investigated the possible role of mixed-layer depth on regulating PB. If deepening of the mixed layer in winter can recharge the surface layer in nutrients (iron, but also nitrate and silicic acid in the temperate regimes) by deep convection, it can also limit PB by reducing light availability for phytoplankton growth during the growing season. Indeed, region of deep winter mixing in the Southern Ocean are mostly located directly north of the ACC, where strong winds and isopycnal tilts, are associated with an season-wide weak stratification, leading to deep winter mixed layer but also to relatively deep, compared to their surrounding, spring and summer mixed-layers.

Our findings clearly translate this complex interplay between availability of nutrient and light related to the winter mixed-layer depth. An increase in PB is observed with the deepening of the winter mixed-layer until a maximum winter depth of about 150 m. When the winter mixed

layer becomes deeper, a decrease in PB is observed, likely resulting from a stronger light limitation of phytoplankton growth during the growth season (Sep-Mar; on average, winter mixed layer deeper than 150 m are associated to Sep-Mar mixed layer deeper than 110 m or so; Fig 4b). We thus depict here a tipping winter MLD at ~ 150m, which likely represents a shift between an iron-limited to a light-limited environment. Such threshold in the MLD is certainly dependent on the local structure of the iron profile [*Tagliabue et al.*, 2014b]. Despite the HNLC (High Nutrient Low Chlorophyll) nature of the Southern Ocean, an intermediate mixing mode (i.e., with a winter MLD maximum from 120 to 200 meters) appears to enhance PB by supplying an optimal combination of both light and nutrient requirements for phytoplankton growth. This apparently modest effect of optimal mixing on PB may nevertheless have major implications due to the large areal extension of those zones relying on the vertical mixing to support phytoplankton iron requirements (Fig. 4c).

Deciphering the complexity of the SO's phytoplankton phenology and biomass is particularly critical to assess how climate variability and change might regionally impact the biological pump. Our results reveal two main scales of organization for both PB and PH, i.e. a large latitudinal and a regional scale. Alterations of stratification that are expected with global warming may modify light-mixing regimes, and thus potentially modulate the bloom timing. However, since the phenology appears here to be strongly linked to the circumpolar seasonal cycle in irradiance, we suppose that only drastic changes in stratification could significantly alter bloom timing, and therefore the impact on the biological pump might be expected to be relatively minor.

Concerning the fate of phytoplankton biomass in the changing SO, no particular changes at local scale are expected in shallow bathymetry (i.e. where iron recharge from shallow plateaus

253 (<500 m) are not prone to be affected). Potential changes also likely to remain minor in
254 downstream transport from ACC, depending on whether the ACC has shifted locally in some
255 regions over the past decades according to climate model [*Kim and Orsi*, 2014; *Sallée et al.*,
256 2008] but not others [*Gille*, 2014; *Shao et al.*, 2015]. Even if ACC changes remain unclear under
257 next century climate change scenarios [*Meijers et al.*, 2012], past studies indicate that if there is a
258 change, the expected position change should be small compared to the size of the bathymetry
259 structure it interacts with to give rise to ocean surface iron plumes.

260 The main uncertainties regarding the fate of PB thus remains linked to the role of the
261 mixed-layer depth and the sea-ice, which have a more direct response to climate variability and
262 change. Climate modes have direct regional impact on both sea-ice and mixed-layer depth
263 [*Sallée et al.*, 2010; *Simpkins et al.*, 2012]. In response to SAM and ENSO, sea-ice extends in
264 some regions and is reduced in others, which, according to our results, would have regional
265 impact on iron delivery and PB intensity. Similarly, SAM tends to deepen mixed-layer depth
266 regionally but shallows it in other regions. Under next century climate change, the response is
267 more regionally consistent, with an overall shallowing of the mixed-layer associated with
268 increased stratification (freshwater input from glacier and sea-ice, and increased heat forcing
269 from the atmosphere), and an overall reduction of sea-ice cover.

270 However, according to our findings, a shallowing (or deepening) of the mixed-layer is not
271 expected to translate to the same PB response everywhere (see SI, Fig. S2). Indeed, the response
272 would be state-dependent: a shallowing of a deep mixed-layer (typically deeper than 200 m)
273 would result in an increase in PB, while a shallowing of an already relatively shallow mixed-
274 layer (typically less than 120 m), would reduce PB. At the SO scale, a global shallowing of the
275 mixed-layer depth appears to have negative consequences on PB (loss of ≈0.3 % m^{-1}; see SI),

mainly due to the areal increase of depleted-iron regions with less efficient vertical iron recharge. Conversely, a positive response of PB (increase of ≈0.15 % m^{-1}; see SI) would be observed with a global deepening of the mixed-layer until a critical threshold (+40 m compared to the actual mixed-layer depth climatology), from which severe light limitation damps phytoplankton growth and biomass. Given the more direct response of the MLD to climate variability and change in the SO, these results highlight the crucial role of the local vertical mixing and the associated subtle balance between light/nutrient availability on regulating PB in the majority of the HNLC areas of the SO.

Acknowledgments

The GLOBcolour data were made available by the European Space Agency's GlobColour project (http://www.globcolour.info). The altimetric data was provided by AVISO/CNES from their website http://www.aviso.altimetry.fr/fr/. We gratefully acknowledge the whole OMTAB team for constructive discussion on initial versions of the manuscript. We also thank Bernard Quéguiner and an anonymous reviewer for constructive comments on the manuscript. M.A. received a postdoctoral fellowship from the CNES (Centre National d'Études Spatiales) and the European Research Council (ERC) remOcean project (grant agreement 246777).

Reference

Ardyna, M., M. Babin, M. Gosselin, E. Devred, L. Rainville, and J.-É. Tremblay (2014), Recent Arctic Ocean sea-ice loss triggers novel fall phytoplankton blooms, *Geophys. Res. Lett.*, *41*(17), 6207-6212.

Arrigo, K. R., G. L. van Dijken, and S. Bushinsky (2008), Primary production in the Southern Ocean, 1997-2006, *J. Geophys. Res.*, *113*(C8), C08004.

Arrigo, K. R., G. L. van Dijken, and A. L. Strong (2015), Environmental controls of marine productivity hot spots around Antarctica, *J. Geophys. Res.*, *120*(8), 5545-5565.

Behrenfeld, M., and E. Boss (2014), Resurrecting the Ecological Underpinnings of Ocean Plankton Blooms, *Annu. Rev. Mar. Sci.*, *6*, 167-194.

Boyd, P. W. (2002), Environmental factors controlling phytoplankton processes in the Southern Ocean, *J. Phycol.*, *38*(5), 844-861.

Boyd, P. W., K. R. Arrigo, R. Strzepek, and G. L. van Dijken (2012), Mapping phytoplankton iron utilization: Insights into Southern Ocean supply mechanisms, *J. Geophys. Res.*, *117*(C6), C06009.

Cassar, N., M. L. Bender, B. A. Barnett, S. Fan, W. J. Moxim, H. Levy, and B. Tilbrook (2007), The Southern Ocean Biological Response to Aeolian Iron Deposition, *Science*, *317*(5841), 1067-1070.

D'Ortenzio, F., and M. Ribera d'Alcalà (2009), On the trophic regimes of the Mediterranean Sea: a satellite analysis, *Biogeosciences*, *6*(2), 139-148.

D'Ortenzio, F., D. Antoine, E. Martinez, and M. Ribera d'Alcalà (2012), Phenological changes of oceanic phytoplankton in the 1980s and 2000s as revealed by remotely sensed ocean-color observations, *Global Biogeochem. Cycles*, *26*(4), GB4003.

d'Ovidio, F., A. Della Penna, T. W. Trull, F. Nencioli, M. I. Pujol, M. H. Rio, Y. H. Park, C. Cotté, M. Zhou, and S. Blain (2015), The biogeochemical structuring role of horizontal stirring: Lagrangian perspectives on iron delivery downstream of the Kerguelen Plateau, *Biogeosciences*, *12*(19), 5567-5581.

Dall'Olmo, G., J. Dingle, L. Polimene, R. J. W. Brewin, and H. Claustre (2016), Substantial energy input to the mesopelagic ecosystem from the seasonal mixed-layer pump, *Nature Geosci*, *9*(11), 820–823.

Devred, E., S. Sathyendranath, and T. Platt (2007), Delineation of ecological provinces using ocean colour radiometry, *Mar. Ecol. Prog. Ser.*, *346*, 1-13.

Dobson, F. W., and S. D. Smith (1988), Bulk models of solar radiation at sea, *Q.J.R. Meteorol. Soc.*, *114*(479), 165-182.

Edwards, M., and A. J. Richardson (2004), Impact of climate change on marine pelagic phenology and trophic mismatch, *Nature*, *430*(7002), 881-884.

Fossheim, M., R. Primicerio, E. Johannesen, R. B. Ingvaldsen, M. M. Aschan, and A. V. Dolgov (2015), Recent warming leads to a rapid borealization of fish communities in the Arctic, *Nature Clim. Change*, *5*, 673–677.

Gille, S. T. (2014), Meridional displacement of the Antarctic Circumpolar Current, *Phil. Trans. R. Soc. A.*, *372*(2019), 20130273.

Graham, R. M., A. M. De Boer, E. van Sebille, K. E. Kohfeld, and C. Schlosser (2015), Inferring source regions and supply mechanisms of iron in the Southern Ocean from satellite chlorophyll data, *Deep Sea Research Part I: Oceanographic Research Papers*, *104*, 9-25.

Gregg, W. W., and K. L. Carder (1990), A simple spectral solar irradiance model for cloudless maritime atmospheres, *Limnol. Oceanogr.*, *35*(8), 1657-1675.

Hartigan, J. A., and M. A. Wong (1979), Algorithm AS 136: A K-Means Clustering Algorithm, *J. Roy. Stat. Soc. C-App.*, *28*(1), 100-108.

Hutchins, D. A., and P. W. Boyd (2016), Marine phytoplankton and the changing ocean iron cycle, *Nature Clim. Change*, *6*(12), 1072-1079.

IOCCG (2009), *Partition of the Ocean into Ecological Provinces: Role of Ocean-Colour Radiometry*, International Ocean Colour Coordinating Group, Dartmouth, Canada.

Khatiwala, S., F. Primeau, and T. Hall (2009), Reconstruction of the history of anthropogenic CO2 concentrations in the ocean, *Nature*, *462*(7271), 346-349.

Kim, Y. S., and A. H. Orsi (2014), On the Variability of Antarctic Circumpolar Current Fronts Inferred from 1992–2011 Altimetry, *Journal of Physical Oceanography*, *44*(12), 3054-3071.

Lacour, L., H. Claustre, L. Prieur, and F. D'Ortenzio (2015), Phytoplankton biomass cycles in the North Atlantic subpolar gyre: a similar mechanism for two different blooms in the Labrador Sea, *Geophys. Res. Lett.*, 2015GL064540.

Landschützer, P., et al. (2015), The reinvigoration of the Southern Ocean carbon sink, *Science*, *349*(6253), 1221-1224.

Lannuzel, D., M. Vancoppenolle, P. v. d. Merwe, J. d. Jong, K. M. Meiners, M. Grotti, J. Nishioka, and V. Schoemann (2016), Iron in sea ice: Review and new insights, *Elem Sci Anth*, *4*, 000130.

Le Quéré, C., T. Takahashi, E. T. Buitenhuis, C. Rödenbeck, and S. C. Sutherland (2010), Impact of climate change and variability on the global oceanic sink of CO2, *Global Biogeochemical Cycles*, *24*(4), GB4007.

Legendre, L., and F. Rassoulzadegan (1995), Plankton and nutrient dynamics in marine waters, *Ophelia*, *41*, 153-172.

Longhurst, A. (2007), *Ecological Geography of the Sea (Second Edition)*, Academic Press, Burlington.

Lund, R., and B. Li (2009), Revisiting Climate Region Definitions via Clustering, *J. Climate*, *22*(7), 1787-1800.

Maritorena, S., O. H. F. d'Andon, A. Mangin, and D. A. Siegel (2010), Merged satellite ocean color data products using a bio-optical model: Characteristics, benefits and issues, *Remote Sens. Environ.*, *114*(8), 1791-1804.

Markus, T. (1999), Results from an ECMWF-SSM/I forced mixed layer model of the Southern Ocean, *J. Geophys. Res.*, *104*(C7), 15603-15620.

Mayot, N., F. D'Ortenzio, M. Ribera d'Alcalà, H. Lavigne, and H. Claustre (2016), Interannual variability of the Mediterranean trophic regimes from ocean color satellites, *Biogeosciences*, *13*(6), 1901-1917.

Meijers, A. J. S., E. Shuckburgh, N. Bruneau, J.-B. Sallée, T. J. Bracegirdle, and Z. Wang (2012), Representation of the Antarctic Circumpolar Current in the CMIP5 climate models and future changes under warming scenarios, *J. Geophys. Res.*, *117*(C12), C12008.

Milligan, G., and M. Cooper (1985), An examination of procedures for determining the number of clusters in a data set, *Psychometrika*, *50*(2), 159-179.

Munro, D. R., N. S. Lovenduski, T. Takahashi, B. B. Stephens, T. Newberger, and C. Sweeney (2015), Recent evidence for a strengthening CO2 sink in the Southern Ocean from carbonate system measurements in the Drake Passage (2002–2015), *Geophys. Res. Lett.*, *42*(18), 2015GL065194.

O'Reilly, J., et al. (2000), SeaWiFS Postlaunch Calibration and Validation Analyses, Part 3*Rep.*, NASA Goddard Space Flight Center.

Pellichero, V., J. B. Sallée, S. Schmidtko, F. Roquet, and J. B. Charrassin (2016), The ocean mixed-layer under Southern Ocean sea-ice: seasonal cycle and forcing, *J. Geophys. Res. Oceans*.

Polovina, J. J., E. A. Howell, and M. Abecassis (2008), Ocean's least productive waters are expanding, *Geophys. Res. Lett.*, *35*(3), L03618.

Quéguiner, B. (2013), Iron fertilization and the structure of planktonic communities in high nutrient regions of the Southern Ocean, *Deep Sea Res. Pt. 2*, *90*(0), 43-54.

392 Sallée, J. B., K. Speer, and R. Morrow (2008), Southern Ocean fronts and their variability to
393 climate modes, *J. Climate*, *21*(12), 3020-3039.

394 Sallée, J. B., K. G. Speer, and S. R. Rintoul (2010), Zonally asymmetric response of the Southern
395 Ocean mixed-layer depth to the Southern Annular Mode, *Nature Geosci*, *3*(4), 273-279.

396 Sanial, V., P. van Beek, B. Lansard, F. d'Ovidio, E. Kestenare, M. Souhaut, M. Zhou, and S.
397 Blain (2014), Study of the phytoplankton plume dynamics off the Crozet Islands (Southern
398 Ocean): A geochemical-physical coupled approach, *J. Geophys. Res. Oceans*, *119*(4), 2227-
399 2237.

400 Sanial, V., P. van Beek, B. Lansard, M. Souhaut, E. Kestenare, F. d'Ovidio, M. Zhou, and S.
401 Blain (2015), Use of Ra isotopes to deduce rapid transfer of sediment-derived inputs off
402 Kerguelen, *Biogeosciences*, *12*(5), 1415-1430.

403 Shao, A. E., S. T. Gille, S. Mecking, and L. Thompson (2015), Properties of the Subantarctic
404 Front and Polar Front from the skewness of sea level anomaly, *J. Geophys. Res.*, *120*(7), 5179-
405 5193.

406 Simpkins, G. R., L. M. Ciasto, D. W. J. Thompson, and M. H. England (2012), Seasonal
407 Relationships between Large-Scale Climate Variability and Antarctic Sea Ice Concentration, *J.*
408 *Climate*, *25*(16), 5451-5469.

409 Swart, S., S. Speich, I. J. Ansorge, and J. R. E. Lutjeharms (2010), An altimetry-based gravest
410 empirical mode south of Africa: 1. Development and validation, *J. Geophys. Res.*, *115*(C03002),
411 2156-2202.

412 Tagliabue, A., L. Bopp, and O. Aumont (2009), Evaluating the importance of atmospheric and
413 sedimentary iron sources to Southern Ocean biogeochemistry, *Geophys. Res. Lett.*, *36*(13),
414 L13601.

415 Tagliabue, A., O. Aumont, and L. Bopp (2014a), The impact of different external sources of iron
416 on the global carbon cycle, *Geophys. Res. Lett.*, *41*(3), 920–926.

417 Tagliabue, A., J.-B. Sallée, A. R. Bowie, M. Levy, S. Swart, and P. W. Boyd (2014b), Surface-
418 water iron supplies in the Southern Ocean sustained by deep winter mixing, *Nature Geosci*, *7*(4),
419 314-320.

420 Tagliabue, A., A. R. Bowie, P. W. Boyd, K. N. Buck, K. S. Johnson, and M. A. Saito (2017),
421 The integral role of iron in ocean biogeochemistry, *Nature*, *543*(7643), 51-59.

422 Venables, H. J., A. Clarke, and M. P. Meredith (2013), Wintertime controls on summer
423 stratification and productivity at the western Antarctic Peninsula, *Limnol. Oceanogr.*, *58*(3),
424 1035–1047.

425 Zar, J. (2010), *Biostatistical Analysis, 5th edition*, Pearson Prentice Hall, New Jersey.
426

Figure captions

Figure 1: Phytoplankton biomass, net primary production and phenology in the Southern Ocean. Map showing the climatological (a) annual mean chlorophyll *a* concentration (mg m^{-3}), (b) annual net primary production (g C m^{-2} d^{-1}), (c) the chlorophyll *a* seasonality (mg m^{-3}), (d) the timing of the bloom (week) maximum based on the GLOBcolour time series (1998–2014). The climatological annual net primary production (b; mg C m^{-2} d^{-1}) was derived from the adapted-SO NPP model of Arrigo et al. (2008). Frontal positions calculated from MADT contours are shown for the STF (white), the SAF (red), the PF (yellow) and the SACCF (black).

Figure 2: Biogeography of the Southern Ocean. Spatial distribution (a) of the 7 bio-regions (i.e. bio-regions 1 to 7) of the Southern Ocean obtained from the k-means analysis. The normalized annual chlorophyll cycles (continuous lines) of the centers of the clusters (b − h) obtained from the k-means analysis are presented, as well as their respective standard deviation. The absolute annual chlorophyll cycles (dashed lines) corresponding to the centers of the clusters (b − h) are also indicated.

Figure 3: Latitudinal repartition of the bio-regions and their respective biological characteristics. Latitudinal proportion (a) of the different bio-regions. Box plots of the bio-regions (1 to 7; x axis) against (b) annual mean chlorophyll *a* concentration (mg m^{-3}), (c) the chlorophyll a seasonality (mg m^{-3}), (d) the timing of the bloom maximum (month; y axis). The line in the middle of each box represents the region median. The top and bottom limits of each box are the 25th and 75th percentiles, respectively. The lines extending above and below each

box, i.e., whiskers, represent the full range of non-outlier observations for each variable beyond the quartile range. The results of the Kruskal–Wallis H test are shown in figures (b) through (d), and depict regions with statistically significant differences between the climatological input variables at the 95 % level ($p < 0.05$). The codes of the test significance are as follow .: $p < 0.05$, *: $p < 0.01$, **: $p < 0.001$ and ***: $p < 0.0001$.

Figure 4: Environmental control of phytoplankton biomass and phenology in the Southern Ocean. Double boxplot (a) of the maximum bloom timing (weeks) versus the annual mean PAR (E m y^{-1}) of the different bio-regions. The top/right and bottom/left limits of each box are the 25th and 75th percentiles, respectively. The numbers in each box are located at the median of both maximum bloom timing and annual mean PAR. Barplot (b) of the mean annual chlorophyll *a* concentration according (1) the shallow areas (< 500 m; red), (2) areas where iron delivery downstream take place (%; percent of iron remaining in a water parcel after scavenging in respect to its initial concentration acquired in shallow areas; red to blue), (3) areas characterized by a seasonal sea-ice cover (grey) and (4) areas where variations in the annual maximum MLD are analyzed (white). See the map (c) delineating the distinct areas listed just above.

Figure 1.

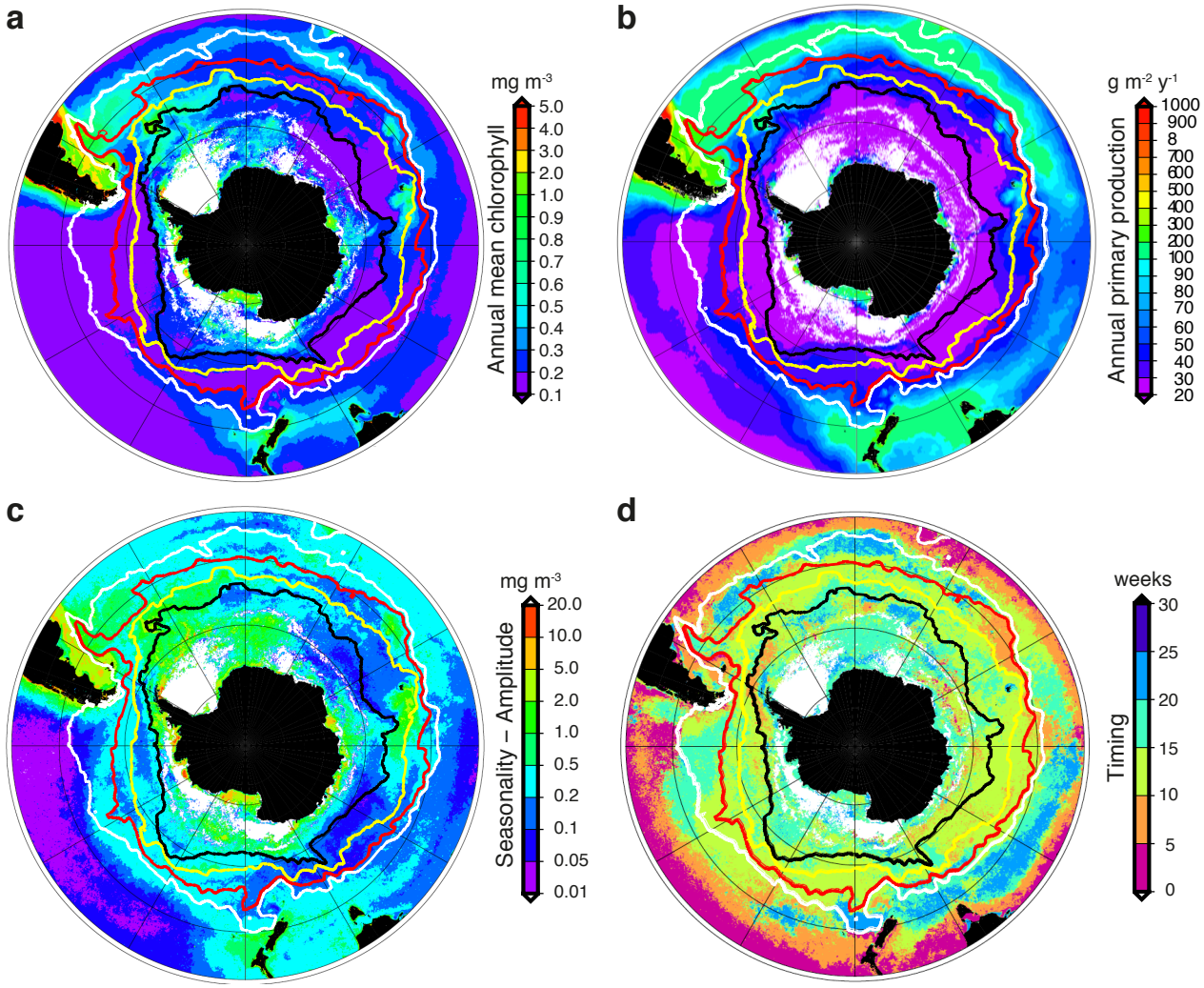
a
mg m-3
Annual mean chlorophyll
5.0
4.0
3.0
2.0
1.0
0.9
0.8
0.7
0.6
0.5
0.4
0.3
0.2
0.1
b
g m-2 y-1
Annual primary production
1000
900
8
700
600
500
400
300
200
100
90
80
70
60
50
40
30
20
c
mg m-3
Seasonality – Amplitude
20.0
10.0
5.0
2.0
1.0
0.5
0.2
0.1
0.05
0.01
d
weeks
Timing
30
25
20
15
10
5
0

Figure 2.

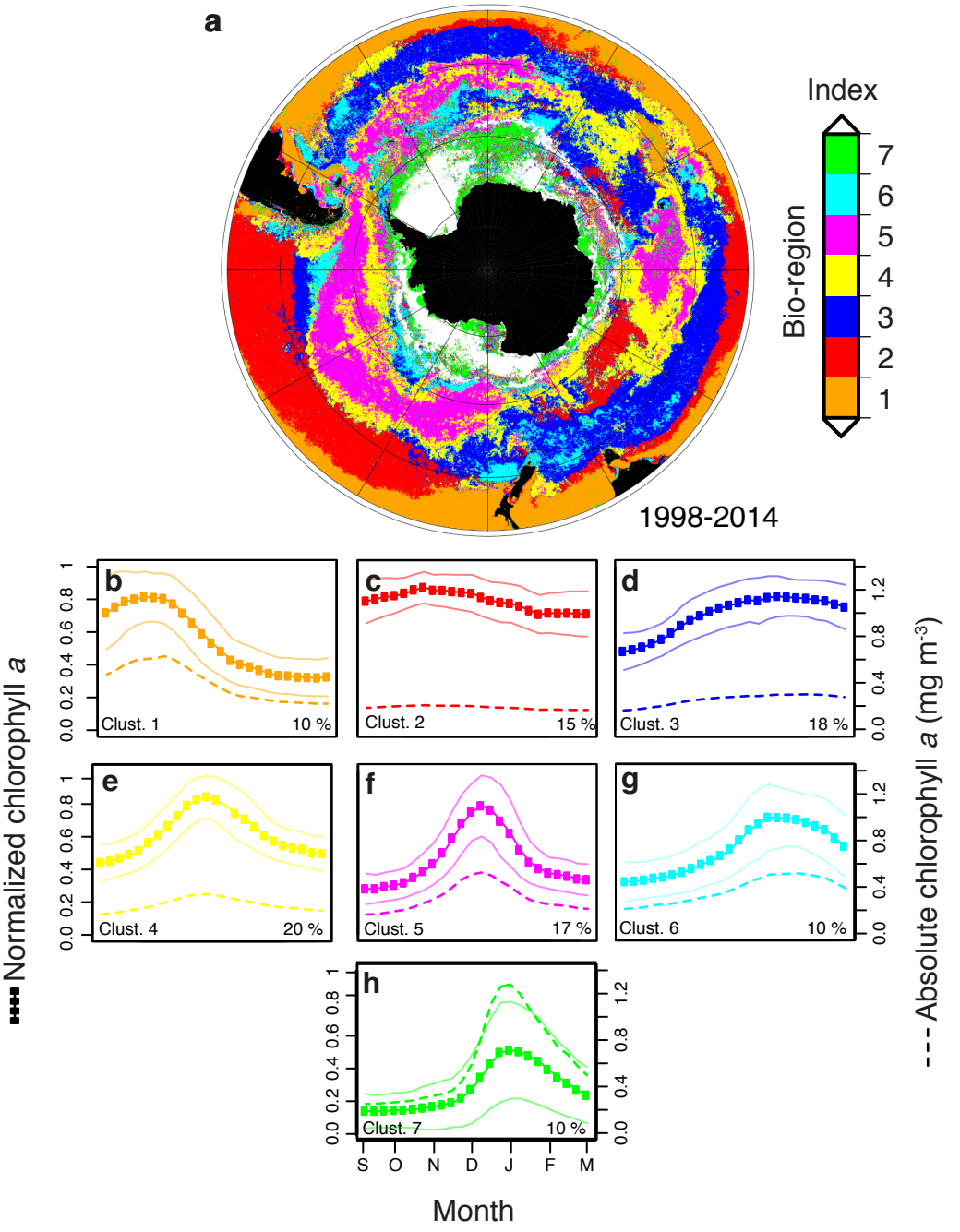
a
Index
Bio-region
7
6
5
4
3
2
1
1998-2014
b
Clust. 1
10 %
c
Clust. 2
15 %
d
Clust. 3
18 %
e
Clust. 4
20 %
f
Clust. 5
17 %
g
Clust. 6
10 %
h
Clust. 7
10 %
0.0 0.2 0.4 0.6 0.8 1
0.0 0.4 0.8 1.2
S O N D J F M
Month
Normalized chlorophyll a
Absolute chlorophyll a (mg m-3)

Figure 3.

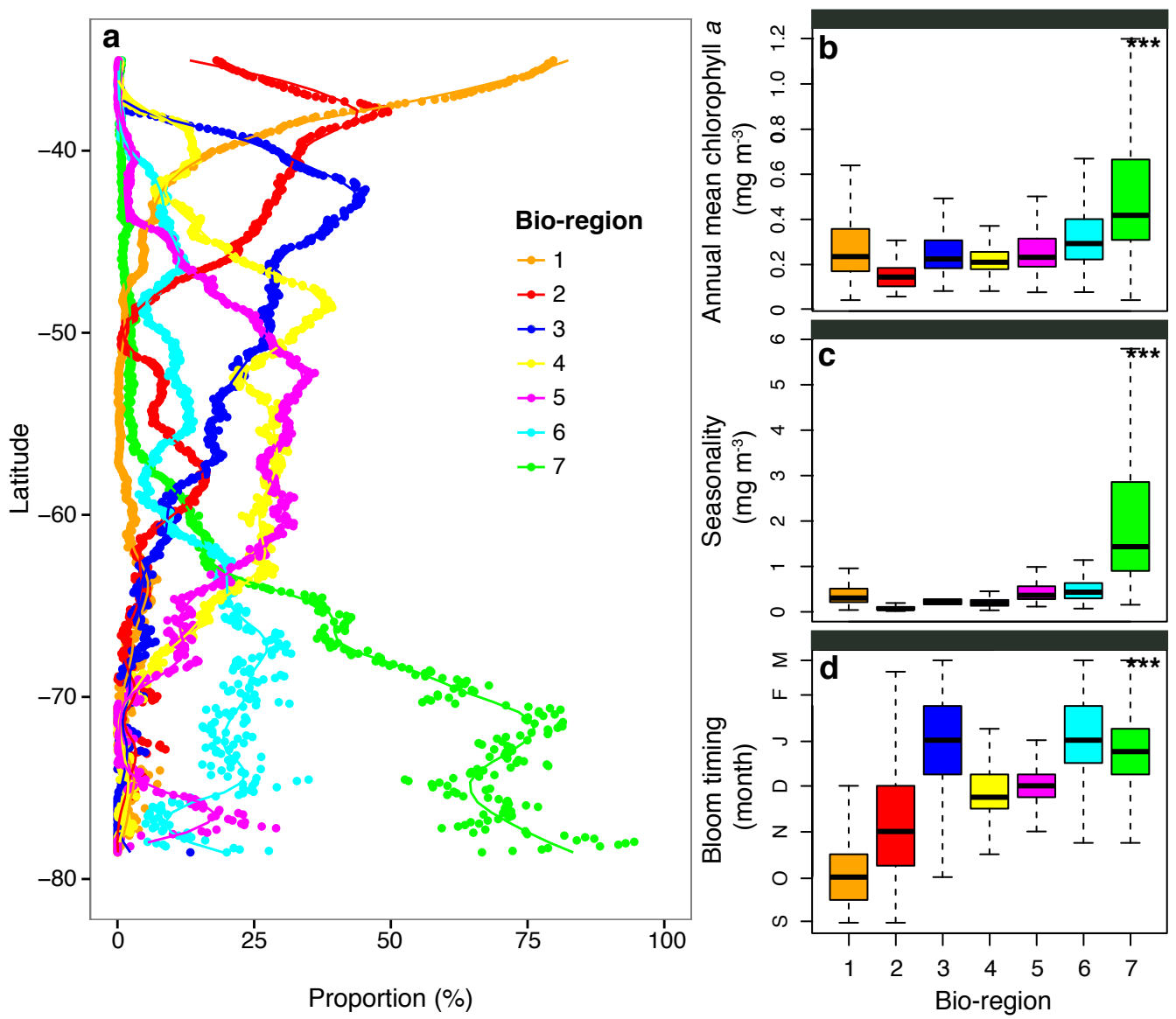
a
Latitude
−40
−50
−60
−70
−80
0
25
50
75
100
Proportion (%)
Bio-region
1
2
3
4
5
6
7
b
Annual mean chlorophyll a (mg m-3)
0
0.2
0.4
0.6
0.8
1.0
1.2
***
c
Seasonality (mg m-3)
0
1
2
3
4
5
6
***
d
Bloom timing (month)
S
O
N
D
J
F
M
***
1
2
3
4
5
6
7
Bio-region

Figure 4.

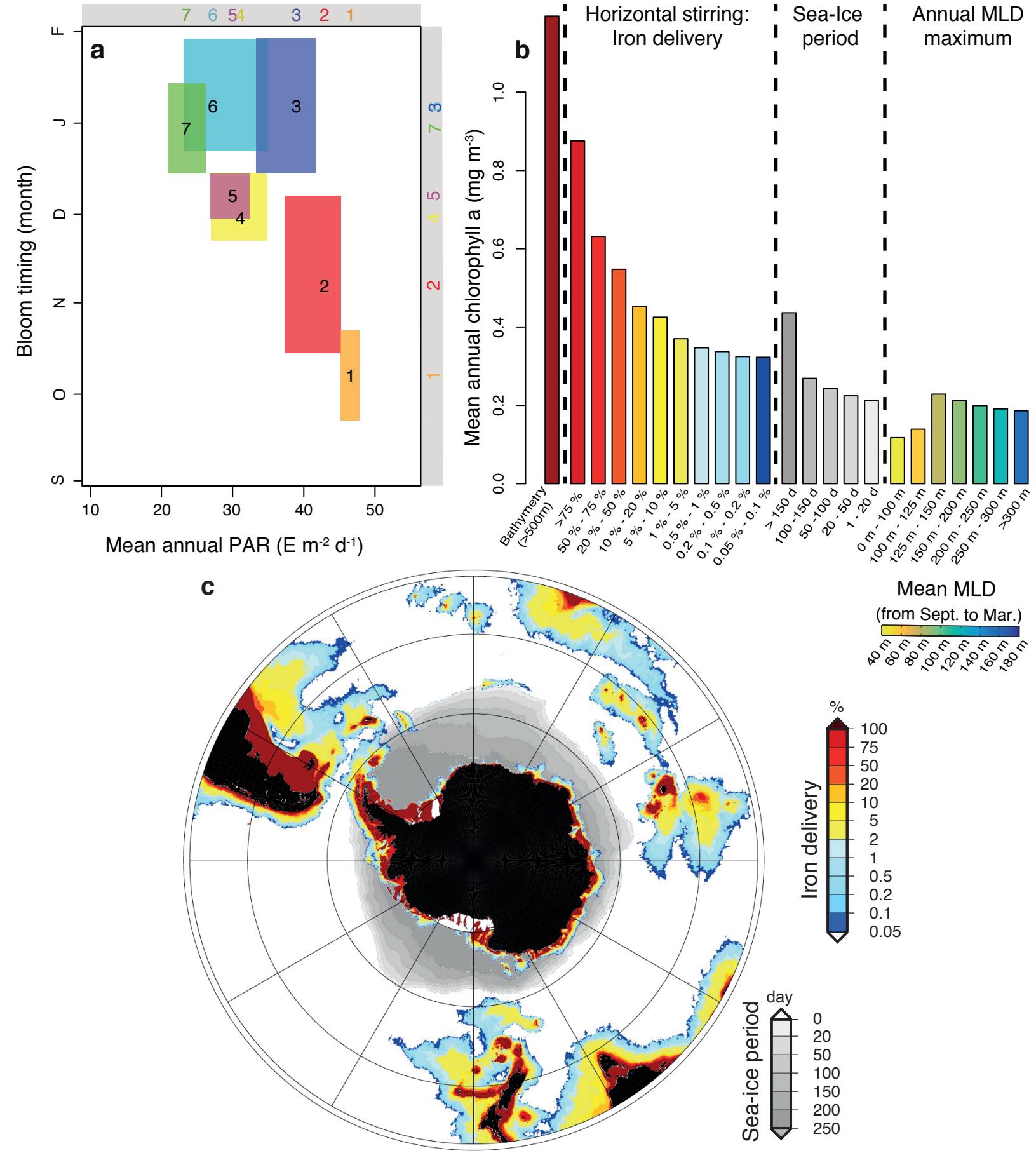
a
Bloom timing (month)
Mean annual PAR (E m-2 d-1)
b
Horizontal stirring: Iron delivery
Sea-Ice period
Annual MLD maximum
Mean annual chlorophyll a (mg m-3)
Bathymetry (>500m)
>75 %
50 % - 75 %
20 % - 50 %
10 % - 20 %
5 % - 10 %
1 % - 5 %
0.5 % - 1 %
0.2 % - 0.5 %
0.1 % - 0.2 %
0.05 % - 0.1 %
> 150 d
100 -150 d
50 -100 d
20 - 50 d
1 - 20 d
0 m - 100 m
100 m - 125 m
125 m - 150 m
150 m - 200 m
200 m - 250 m
250 m - 300 m
>300 m
c
Mean MLD
(from Sept. to Mar.)
40 m
60 m
80 m
100 m
120 m
140 m
160 m
180 m
Iron delivery
%
100
75
50
20
10
5
2
1
0.5
0.2
0.1
0.05
Sea-ice period
day
0
20
50
100
150
200
250